vibration

MDPI

Article

Modeling Hysteretically Nonlinear Piezoelectric Composite Beams

Abdulaziz H. Alazemi * and Andrew J. Kurdila

Department of Mechanical Engineering, Virginia Tech, Blacksburg, VA 24061, USA; kurdila@vt.edu
* Correspondence: alduwaihees@vt.edu

Abstract

This paper presents a modeling framework for hysteretically nonlinear piezoelectric composite beams using functional differential equations (FDEs). While linear piezoelectric models are well established, they fail to capture the complex nonlinear behaviors that emerge at higher electric field strengths, particularly history-dependent hysteresis effects. This paper develops a cascade model that integrates a high-dimensional linear piezoelectric composite beam representation with a nonlinear Krasnosel'skii–Pokrovskii (KP) hysteresis operator. The resulting system is formulated using a state-space model where the input voltage undergoes a history-dependent transformation. Through modal expansion and discretization of the Preisach plane, we derive a tractable numerical implementation that preserves essential nonlinear phenomena. Numerical investigations demonstrate how system parameters, including the input voltage amplitude, and hysteresis parameters significantly influence the dynamic response, particularly the shape and amplitude of limit cycles. The results reveal that while the model accurately captures memory-dependent nonlinearities, it depends on numerous real and distributed parameters, highlighting the need for efficient reduced-order modeling approaches. This work provides a foundation for understanding and predicting the complex behavior of piezoelectric systems with hysteresis, with potential applications in vibration control, energy harvesting, and precision actuation.

Keywords: piezoelectric composites; hysteresis modeling; functional differential equations; Krasnosel'skii–Pokrovskii operator; nonlinear dynamics; limit cycles; smart materials

check for updates

Academic Editors: Francesco Pellicano, Yuri Mikhlin, Konstantin V. Avramov and Antonio Zippo

Received: 26 May 2025
Revised: 26 June 2025
Accepted: 2 July 2025
Published: 6 July 2025

Citation: Alazemi, A.H.; Kurdila, A.J. Modeling Hysteretically Nonlinear Piezoelectric Composite Beams. *Vibration* **2025**, *8*, 37. https://doi.org/10.3390/vibration8030037

Copyright: © 2025 by the authors. Licensee MDPI, Basel, Switzerland. This article is an open access article distributed under the terms and conditions of the Creative Commons Attribution (CC BY) license (https://creativecommons.org/licenses/by/4.0/).

1. Introduction

Active materials respond to external stimuli by changing their properties or converting energy from one form to another. Among them, piezoelectric materials generate electrical energy under mechanical load and deform under applied electric fields, making them essential in sensing and actuation applications [1]. In contrast, shape-memory alloys (SMAs) respond to thermal changes and are widely used in medical devices and actuators, while magnetostrictive, electrorheological, and magnetorheological materials have diverse industrial applications [1,2].

This work focuses on active structural systems based on piezoelectric materials, which enable bidirectional energy conversion through the direct and converse piezoelectric effects [1–5]. Due to their high sensitivity to mechanical and electrical variations, piezoelectric composites are extensively used in vibration control, sensing, and energy harvesting. They play a central role in transducers, such as force, pressure, and acoustic sensors, and in actuators for microelectromechanical systems (MEMSs) and energy harvesters [1–6].

The theory of linear piezoelectric materials is well established and can be found in standard works [4,5,7]. However, modeling piezoelectric systems becomes significantly more complex under nonlinear effects arising from large electric fields, mechanical strain, or thermal conditions. These nonlinearities often require higher-order terms or nonlinear constitutive laws to accurately describe the system dynamics [3,4,8]. While some models treat the electromechanical coupling as linear, nonlinear modeling often yields more accurate predictions and can exploit beneficial system behaviors.

A broad class of nonlinear models incorporates polynomial terms into the constitutive relationships. For instance, a first-principles model that includes higher-order elastic effects, nonlinear damping, and circuit coupling was developed in [9], where experimental validation confirmed its accuracy for frequency response prediction. Similarly, quadratic nonlinearities were shown in [10] to effectively capture the dynamic behavior of piezoelectric bimorph cantilevers.

Other works explore nonlinear piezoelectricity in the context of smart damping and control. The use of nonlinear models to evaluate the frequency response of partially covered cantilevers connected to SSDI circuits is demonstrated in [11], while the authors of [12] compared two nonlinear piezoelectric models to improve vibration attenuation at low frequencies. In both cases, experimental measurements validate the enhanced performance predicted by nonlinear modeling. In addition, the authors of [13] developed and validated a nonlinear smart beam energy harvester with a shunt controller.

Another important class of nonlinearities in piezoelectric electromechanical systems arises from hysteresis, where the system output depends not only on the current input but also on its past history [14]. Hysteresis is observed in mechanical, electrical, and electromechanical coupling elements and can introduce significant challenges such as reduced control accuracy, increased power consumption, and instability [15]. Consequently, modeling hysteresis is essential for effective control and compensation strategies.

Several mathematical models have been developed to describe hysteresis behavior in electromechanical systems. These include the Preisach model, based on a superposition of elementary hysterons; the Bouc-Wen model, formulated using nonlinear differential equations; the Prandtl–Ishlinskii model, which uses series of play and stop operators; and the Krasnosel'skii–Pokrovskii (KP) model, which defines hysteresis via integral operators with specific kernels [14–16]. The choice among these models typically depends on the trade-off between accuracy and computational complexity.

From a broader mathematical perspective, history-dependent behavior can also be modeled using functional differential equations, differential inclusions, or history-dependent operators [14,16–19]. These frameworks are particularly suited for capturing the long-term memory effects inherent in piezoelectric systems but introduce further complexity in analysis and simulation.

Recent studies have incorporated such hysteresis models into experimental and control frameworks. For instance, the authors of [20] introduced a robust output-feedback controller that compensates for actuator hysteresis, while the authors of [21] proposes a modified Prandtl–Ishlinskii model integrated with sliding mode control to enhance the tracking performance of piezoelectric actuators.

Foundational texts on piezoelectricity and smart material systems provide the theoretical framework for modeling electromechanical structures, covering constitutive theory, parameter estimation, Galerkin approximation, and finite dimensional control synthesis [1,3–5,8]. In the context of energy harvesting, Erturk and Inman [6] presented analytical models of cantilever-based piezoelectric systems, validating them under various dynamic loading conditions.

Although the principles of linear piezoelectricity have long been used to derive models for active composites [1,5–7], it is well known that nonlinear effects, particularly under high electric fields, can significantly influence system behavior [6,17,22]. These nonlinearities, which are often poorly understood, complicate the modeling process. Two primary classes of nonlinear modeling approaches have emerged: those addressing polynomial-type nonlinearities and those focused on hysteretic, history-dependent behavior. This paper is concerned with the latter.

Numerous studies have explored the complex hysteretic behavior inherent in piezoelectric actuators, emphasizing the diversity of modeling strategies and the challenges posed by rate dependence, asymmetric loop formation, and multi-scale memory effects. Sabarianand et al. [15] provided a comprehensive review of classical and contemporary hysteresis models, including the Preisach, Bouc–Wen, Prandtl–Ishlinskii and Krasnosel'skii–Pokrovskii operators, highlighting their respective mathematical formulations, implementation trade-offs, and applicability to various actuation scenarios. Their survey underscores the need for tailored models that balance accuracy, generalizability, and computational efficiency, depending on the target application. More recently, Dai et al. [23] surveyed nonlinear modeling efforts specifically for piezoelectric ceramic actuators, emphasizing the limitations of traditional models in capturing dynamic and coupled electromechanical behaviors. They outline modern approaches incorporating neural networks, fractional calculus, and hybrid physics-based and data-driven techniques to better reflect real-world complexities such as temperature sensitivity and loading history. Together, these reviews reflect the growing understanding that hysteresis in piezoelectric systems is not only nonlinear and memory-dependent but also deeply context-specific, necessitating advances in modeling frameworks that can be generalized yet tractable for control and analysis.

Recent studies continue to advance the modeling and control of hysteretically nonlinear behavior in piezoelectric actuators, particularly for precision applications. Xu et al. [24] proposed a fractional-order model that captures both hysteresis and creep effects using non-integer derivatives, offering improved accuracy and reduced parameter complexity compared with classical models like the Bouc–Wen or Preisach models. Their coupled model, validated experimentally, shows significant improvements in tracking performance under sinusoidal and triangular excitations. Similarly, Li et al. [25] developed a hybrid hysteresis model by combining the Preisach–Ishlinskii formulation with a GA-optimized BP neural network. This approach, paired with a fuzzy PID controller, effectively compensates for nonlinearity while enhancing stability and precision across a wide range of frequencies. Baziyad et al. [26] addressed rate-dependent hysteresis by modifying the Preisach model through least squares support vector machines and particle swarm optimization, integrated within a two-degree-of-freedom H_∞ robust control framework. Their experiments confirm superior tracking accuracy and robustness under dynamic loading. Although these works emphasize low-dimensional control performance, they rely on lumped-parameter or black box representations, which limits their ability to capture the distributed-parameter dynamics of real composite structures. This highlights the need for high-fidelity, spatially distributed models that integrate hysteresis effects directly into the governing equations of the structural system, a gap that the present study aims to address.

The primary objective of this study is to develop a modeling framework that captures the hysteretically nonlinear behavior of piezoelectric composite beams using a discretized Preisach-type operator integrated into distributed-parameter dynamics. While classical hysteresis models (e.g., Preisach, Bouc–Wen, and Prandtl–Ishlinskii) are widely used, they are rarely embedded directly into high-dimensional structural models, especially for composite configurations. Moreover, the influence of hysteresis parameters, such as the loop smoothness control (scaling factor) and weighting parameter, on system dynamics and

limit cycle behavior remains poorly understood. Existing approaches often trade accuracy for simplicity or become computationally impractical. This work addresses these gaps by offering a tractable yet detailed framework suitable for analysis and future reduction or data-driven extensions.

The novelty of this work lies in three key aspects. First, we present a modeling framework that integrates rate-independent hysteresis, described by a discretized Preisach-type operator, directly into the dynamics of a distributed-parameter piezoelectric composite beam. This coupling results in a high-dimensional system that captures both the structural response and memory-dependent nonlinear effects. Second, we perform a systematic numerical study to investigate how variations in the hysteresis parameters, such as the loop smoothness control (scaling factor) and weighting parameter (kernel weight) of hysteresis and switching thresholds, influence the steady-state behavior of the system, including the formation and shape of limit cycles. Finally, the resulting model takes the form of a nonlinear functional differential equation (FDE). This formulation provides a general framework for modeling hysteretically nonlinear piezoelectric systems and highlights the computational challenges that motivate future reduced-order or data-driven modeling approaches. The mathematical formulation and coupling methodology are described in detail in Section 2, where the hysteresis operator is introduced into the governing PDE through the external forcing term, resulting in a nonlinear functional differential equation.

2. The Nonlinear System

In this section we discuss the structure of the nonlinear system studied in this paper, which has the overall form shown in Figure 1. It combines a high-dimensional linear model of a piezoelectric composite and a hysteretically nonlinear model.

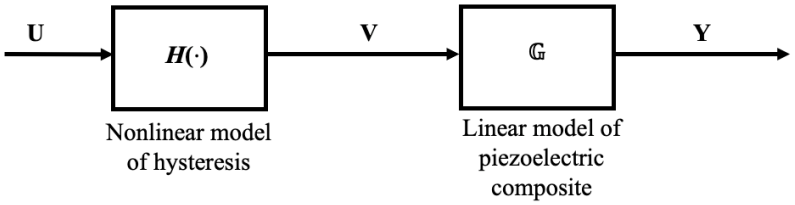

Figure 1. The nonlinear system that is a cascade of a nonlinear hysteresis model and a linear piezoelectric model.

The cascade model is $\mathbb{G} \circ H$, where $\mathbb{G}$ is a model of a linearly piezoelectric composite acting on the hysteresis operator H. In Section 2.1.3, we explicitly derive the state-space representation for the linear model $\mathbb{G}$:

$$\begin{aligned} \dot{\mathbf{X}}(t) &= \mathbb{A}\mathbf{X}(t) + \mathbb{B}\mathbf{V}(t) \\ \mathbf{Y}(t) &= \mathbb{C}\mathbf{X}(t), \end{aligned} \tag{1}$$

so that

$$\mathbb{G}(s) = \mathbb{C}(s\mathbb{I} - \mathbb{A})^{-1}\mathbb{B}. \tag{2}$$

Here, the state vector $X(t) \in \mathbb{R}^{N\times 1}$, the vector of measurements $Y(t) \in \mathbb{R}^{L\times 1}$, the system matrix $\mathbb{A} \in \mathbb{R}^{N\times N}$, the control influence matrix $\mathbb{B} \in \mathbb{R}^{N\times 1}$, the observation matrix $\mathbb{C} \in \mathbb{R}^{L\times N}$, and N is the number of states.

We finally combine the state space and the hysteresis model to obtain the governing equations:

$$\begin{aligned} \dot{\mathbf{X}}(t) &= \mathbb{A}\mathbf{X}(t) + \mathbb{B}\mathbf{H}(\mathbf{U})(t) \\ \mathbf{Y}(t) &= \mathbb{C}\mathbf{X}(t), \end{aligned} \tag{3}$$

where the state $\mathbf{X}(t) \in \mathbb{R}^{N\times 1}$, the input voltage $\mathbf{U}(t) \in \mathbb{R}$, the measured outputs $\mathbf{Y}(t) \in \mathbb{R}^{L\times 1}$, the state matrix $\mathbb{A} \in \mathbb{R}^{N\times N}$, the control influence operator $\mathbb{B} \in \mathbb{R}^{N\times 1}$, and the observation matrix $\mathbb{C} \in \mathbb{R}^{L\times N}$. The history dependence is modeled in terms of the hysteresis operator $\mathbf{H}$, which maps the past history of the input $\{\mathbf{U}(\tau)\}_{\tau\in[0,t]}$ to its output $(\mathbf{HU})(t) \in \mathbb{R}$. This means that the operator representing the hysteresis is a mapping $\mathbf{H} : C([0,t),\mathbb{R}) \mapsto \mathbb{R}$, where $C([0,t),\mathbb{R})$ is the set of real-valued continuous functions on $[0,t)$. As depicted in Figure 1, this model can be understood as a linear or nonlinear cascade of models. Because of the type of hysteresis operator employed in this paper, these equations are examples of nonlinear FDEs and not ordinary differential equations (ODEs). The hysteresis operator H is described in Section 2.2.

2.1. Linear Piezoelectric System

In this paper, a composite cantilever beam, shown in Figure 2, is subjected to an input voltage V. An active composite beam having this structure is commonly known also as a bimorph. The bimorph cantilever beam in Figure 2 has a length L, width b, and thickness h. It consists of a central linearly elastic layer with a thickness h_c and two piezoelectric layers with a thickness h_p on either side. The structure is cantilevered at one end and free at the other, and it is subject to a voltage $2V(t)$ across the piezoelectric layers. The electric potential at the top surface of the piezoelectric layer is Φ^+, while the potential for the bottom surface is Φ^-.

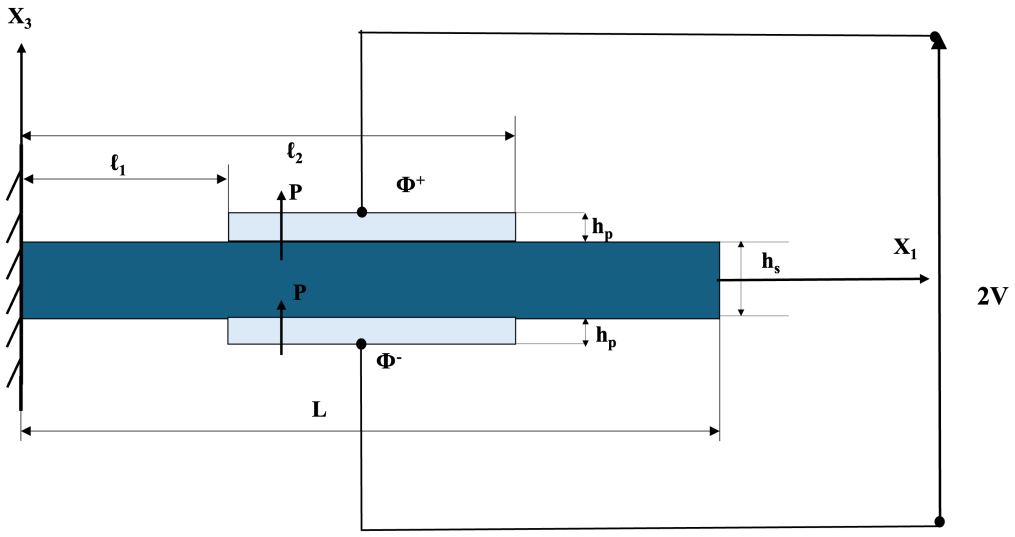

Figure 2. Schematic of a piezoelectric composite beam with surface-bonded piezoelectric actuators. The main structure is a uniform cantilever beam (dark blue) to which two piezoelectric layers are symmetrically bonded to the top and bottom surfaces. The beam is fixed at the left end and free at the right end. The symbol P indicates the direction of polarization of the piezoelectric materials, which is aligned vertically through the thickness of the actuators. When a voltage is applied across the piezoelectric layer (light blue), the induced strain generates bending moments that actuate the host beam. This configuration is commonly used in active vibration control, structural health monitoring, and precision positioning applications.

2.1.1. Background Theory for Linear Piezoelectricity

In this section, we review a beam model for an active piezoelectric composite. We can write the approximate form of the constitutive law for the piezoelectric as follows:

$$\begin{pmatrix} T_{11} \\ D_3 \end{pmatrix} = \begin{pmatrix} C_{11}^E & -e_{31} \\ e_{31} & \varepsilon_{33}^S \end{pmatrix} \begin{pmatrix} S_{11} \\ E_3 \end{pmatrix}, \tag{4}$$

where T_{11} is the bending stress in the x_1 direction, D_3 is the electric displacement in the x_3 direction, E_3 is the electric field in the x_3 direction, S_{11} is the bending strain in the x_1 direction, C_{11}^E is the piezoelectric stiffness, e_{31} is the piezoelectric coupling constant, and ε_{33}^S is the electric permittivity. We approximate the electric field to be

$$E_3(x_1, x_3) = \begin{cases} -\frac{V(t)}{h_p} & \text{if } (x_1, x_3) \in [\ell_1, \ell_2] \times [h_s, h_s + h_p] \\ \frac{V(t)}{h_p} & \text{if } (x_1, x_3) \in [\ell_1, \ell_2] \times [-h_s - h_p, -h_s] \end{cases}, \tag{5}$$

Hamilton's principle for an electromechanical system is used to derive the governing equation of the piezoelectric composite. The governing equations satisfy the variational condition

$$\delta \int_{t_0}^{t_1} (T - V_H) dt + \int_{t_0}^{t_1} \delta W dt = 0, \tag{6}$$

where T represents the kinetic energy, V_H denotes the electrical enthalpy, and δW is the virtual work due to non-conservative electromechanical loads. The kinetic energy is expressed as follows:

$$T = \frac{1}{2} \rho A \int_0^L \left(\frac{\partial w(x,t)}{\partial t} \right)^2 dx, \tag{7}$$

where ρ is the mass density of the beam, A represents the cross-sectional area of the beam, and $w(t, x)$ denotes the deflection of the beam as a function of time t and position x. The electric enthalpy density is approximated as follows:

$$H \approx \frac{1}{2} C_{11}^E S_{11}^2 - e_{31} S_{11} E_3 - \frac{1}{2} \varepsilon_{33}^S E_3^2, \tag{8}$$

and for a Bernoulli–Euler beam, we approximate the bending stress as follows:

$$S_{11} = -x_3 \frac{\partial^2 w}{\partial x_1^2}. \tag{9}$$

We integrate the electric enthalpy over the volume

$$V_H = \int \int \int_V \left(\frac{1}{2} C_{11}^E S_{11}^2 - e_{31} S_{11} E_3 - \frac{1}{2} \varepsilon_{33}^S E_3^2 \right) dx_1 \, dx_2 \, dx_3, \tag{10}$$

and by further simplifying Equation (9), we get

$$V_H = \frac{1}{2} \int_0^L \left\{ C_{11}^E I \left(\frac{\partial^2 w}{\partial x_1^2} \right)^2 - (h_s + h_p) b \frac{\partial^2 w}{\partial x_1^2} \chi_{[\ell_1, \ell_2]} V - \frac{\varepsilon_{33}^S b \chi_{[\ell_1, \ell_2]}^2 V^2}{2 h_p} \right\} dx. \tag{11}$$

In this expression, I is the second area moment of inertia, and $\chi_{[\ell_1, \ell_2]}$ is the characteristic function of the domain. It equals one when χ is within the interval $[\ell_1, \ell_2]$ and is zero otherwise. By applying Hamilton's principle to the kinetic energy, we have

$$\int_{t_0}^{t_1} \delta T = \int_{t_0}^{t_1} \int_0^L -\rho A \ddot{w} \delta w \, dx \, dt. \tag{12}$$

For the electrical enthalpy, we consider V to be prescribed, and therefore $\delta V = 0$. After setting the parameters $\ell_1 = 0$ and $\ell_2 = L$, we align our analysis with the methodology and results presented in [6]. We consequently get

$$\begin{aligned}\delta \int_{t_0}^{t_1} V_H = {} & C_{11}^E I \int_{t_0}^{t_1} \left(w'' \delta w'\right)\Big|_0^L - C_{11}^E I \int_{t_0}^{t_1} \left(w''' \delta w\right)\Big|_0^L \\ & + C_{11}^E I \int_{t_0}^{t_1} \int_0^L w'''' \delta w \, dx \, dt \\ & - \frac{1}{2}\left(h_s + h_p\right) b e_{31} V \int_{t_0}^{t_1} \delta w' \Big|_0^L dt \\ & + \frac{1}{2}\left(h_s + h_p\right) b e_{31} V \int_{t_0}^{t_1} \frac{\partial}{\partial x} \chi_{[0,L]} \delta w \Big|_0^L dt \\ & - \frac{1}{2}\left(h_s + h_p\right) b e_{31} V \int_{t_0}^{t_1} \int_0^L \frac{\partial^2}{\partial x^2} \chi_{[0,L]} \delta w \, dx \, dt. \end{aligned} \tag{13}$$

Considering the damping coefficient C which captures dissipative forces proportional to the velocity, the Hamiltonian becomes

$$\begin{aligned}\delta \int_{t_0}^{t_1} (T - V_H)\, dt = {} & \int_{t_0}^{t_1} \int_0^L \left\{ -\rho A \ddot{w} - c\dot{w} - C_{11}^E I w'''' \right\} \delta w \, dx \, dt \\ & + \frac{1}{2} \int_{t_0}^{t_1} \int_0^L (h_s + h_p) b e_{31} V \frac{\partial^2}{\partial x^2} \chi_{[0,L]} \delta w \, dx \, dt \\ & - C_{11}^E I \left(w'' \delta w' \big|_0^L - w''' \delta w \big|_0^L \right) \\ & + \frac{1}{2} (h_s + h_p) b e_{31} V \chi_{[0,L]}\, \delta w' \big|_0^L \\ & - \frac{1}{2} (h_s + h_p) b e_{31} V \frac{\partial}{\partial x} \chi_{[0,L]} \delta w \Big|_0^L = 0. \end{aligned} \tag{14}$$

Therefore, we have the equation of motion

$$\rho A \ddot{w} + c\dot{w} + C_{11}^E I w'''' - \frac{1}{2}(h_s + h_\rho) b e_{31} V \frac{\partial^2}{\partial x^2} \chi_{[0,L]} = 0, \tag{15}$$

subject to the boundary conditions

$$C_{11}^E I\, w'' \delta w' \big|_0^L + \frac{1}{2}(h_s + h_p) b e_{31} V \chi_{[0,L]}\, \delta w' \big|_0^L = 0, \tag{16}$$

and

$$C_{11}^E I\, w''' \delta w \big|_0^L - \frac{1}{2}(h_s + h_p) b e_{31} V \frac{\partial}{\partial x} \chi_{[0,L]} \delta w \Big|_0^L = 0, \tag{17}$$

and the initial conditions $w(0, x) = w_0(x)$ and $\dot{w}(0, x) = v_0(x)$ for all $x \in \Omega$.
This system has been studied in many works [5,6,9].

2.1.2. Approximation of the PDE

The partial differential equation in Equation (15) must be approximated in practice. The assumed mode methods model the transverse deflection function $w(x, t)$ in terms of a summation of n generalized coordinate displacement functions $q_i(t)$ multiplied by the basis function $P_i(x)$. Common choices include finite element shape functions or eigenfunctions [5]. We then have

$$w(x, t) = \sum_{i=1}^{n} q_i(t) P_i(x), \tag{18}$$

where n is the number of modes and the length of $q(t)$, where $q(t) \in \mathbb{R}^{n\times 1}$.

In this paper, we choose for the basis functions to be eigenfunctions $P_i(x) \triangleq \psi_i(x)$ ([27] Table 6.6, p. 539) which satisfy the orthogonality conditions

$$\int_0^L \psi_i \psi_j dx = \begin{cases} 0 & \text{for } i \neq j, \\ 1 & \text{for } i = j, \end{cases} \tag{19}$$

Using the eigenfunctions, the approximation of the governing PDEs generates the set of decoupled ODEs

$$M\ddot{q}(t) + C\dot{q}(t) + Kq(t) = BV(t). \tag{20}$$

where the mass matrix $M \in \mathbb{R}^{n\times n}$, the stiffness matrix $K \in \mathbb{R}^{n\times n}$, and the control influence vector $B \in \mathbb{R}^{n\times 1}$ are, respectively, as follows:

$$M_{ij} = \int_0^L \rho_e A_t \psi_i \psi_j \, dx = \rho_e A_t diag(m_i), \tag{21}$$

$$K_{ij} = \int_0^L C_e I_t \frac{d^2\psi_i}{dx^2} \frac{d^2\psi_j}{dx^2} \, dx = C_e I_t diag(k_i), \tag{22}$$

$$B_i = \int_0^L \frac{Ke_{31}\chi_{[0,L]}}{h_p} \frac{d^2\psi_i}{dx^2} \, dx. \tag{23}$$

In these equations, ρ_e is the effective density, A_t is the total area, C_e is the effective modulus of elasticity, I_t is the total inertia, m_i is the i^{th} model mass, and k_i is the i^{th} model stiffness. We assume that $C_{ij} = \text{diag}(c_i)$, where c_i is the i^{th} model damping.

2.1.3. State Space Representation

When considering a mechanical system bounded by piezoelectric material and influenced by a control voltage that exhibits hysteresis, we propose the following state-space representation. The approximate dynamic behavior of the system by the system of second-order ODEs is

$$\mathbf{M}\ddot{\mathbf{q}}(t) + \mathbf{C}\dot{\mathbf{q}}(t) + \mathbf{K}\mathbf{q}(t) = \mathbf{B}V(t)$$

where the degrees of freedom $q(t) \in \mathbb{R}^{n\times 1}$, $\mathbf{M} \in \mathbb{R}^{n\times n}$ denotes the mass matrix, $\mathbf{C} \in \mathbb{R}^{n\times n}$ is the damping matrix, $\mathbf{K} \in \mathbb{R}^{n\times n}$ is the stiffness matrix, and $B \in \mathbb{R}^{n\times 1}$ is the control influence vector. V is the control voltage. The state vector $\mathbf{X}$ is defined in the usual way:

$$\mathbf{X}(t) = \begin{bmatrix} q(t) \\ \dot{q}(t) \end{bmatrix},$$

We set N = 2n, and we define the matrices

$$\mathbb{A} = \begin{bmatrix} 0 & \mathbb{I} \\ -\mathbf{M}^{-1}\mathbf{K} & -\mathbf{M}^{-1}\mathbf{C} \end{bmatrix} \in \mathbb{R}^{n\times n}, \quad \mathbb{B} = \begin{bmatrix} 0 \\ \mathbf{M}^{-1}\mathbf{B} \end{bmatrix} \in \mathbb{R}^{n\times 1},$$

These choices yield the state-space equations

$$\dot{\mathbf{X}}(t) = \mathbb{A}\mathbf{X}(\mathbf{t}) + \mathbb{B}V(t).$$

Since n is the number of modes ψ_i, therefore, the number of states $N = 2n$ may be large. On the other hand, the number of measurements L is ordinarily small. We define the L outputs in $\mathbf{Y}(t)$ as follows:

$$\mathbf{Y}(t) = \begin{bmatrix} y_1(t) \\ y_2(t) \\ \vdots \\ y_L(t) \end{bmatrix} = \mathbb{C}\mathbf{X}(t), \quad \text{where } \mathbb{C} \in \mathbb{R}^{L \times N}.$$

2.2. Hysteretically Nonlinear Model

Hysteresis is a well-documented nonlinear phenomenon [14,16]. It presents intricacies in its modeling due to complex relationship between the input and output. Hysteresis is a rate-independent, history-dependent nonlinearity in the system, and there are many approaches to modeling it. Modeling can be based on analytical methods such as ordinary or partial differential equations [14,16].

In this paper, we define a specific history-dependent operator H. Hysteresis is defined in terms of integral operators constructed from certain "building block" history-dependent kernels acting on the input as described in [19,28].

In mathematical terms, the input–output relationship can be described by the operator equation

$$V(t) = (HU)(t),$$

where $U(t)$ is the input at time t, $V(t)$ is the output at time t, and the operator H is a mapping $H : C([0,t],\mathbb{R}) \to \mathbb{R}$. In this study, hysteresis is modeled as a nonlinear transformation of the external input history $\{U(\tau) \mid \tau \in [0,t]\}$ into the output voltage $V(t) \in \mathbb{R}$, which acts as a forcing term in a linear system. This approach separates hysteretic effects from the state dynamics of the piezoelectric material, focusing on systems where hysteresis primarily affects the actuation signal. By treating $V(t)$ as an effective representation of the input after being shaped by the hysteresis operator H, we simplify the modeling process while retaining essential nonlinear characteristics. This cascade formulation assumes that hysteresis is dominated by the input $U(t)$, with minimal feedback from the system state $\mathbf{X}(\mathbf{t})$ to the operator. While this limits the ability to capture state-dependent memory effects in autonomous systems, it provides a practical framework for studying input–output interactions and facilitates reduced-order modeling. The novelty lies in the integration of hysteresis as a history-dependent transformation of the forcing term, enabling efficient state-space representation and the application of linear control techniques. In other words, the operator H maps the history of the input $\{U(\tau) \mid \tau \in [0,t]\}$ up to time t to generate the output $V(t) \in \mathbb{R}$.

The hysteresis operator H is constructed from the superposition of hysteresis kernels $k(s_1, s_2, t, U)$, an example of which is depicted in Figure 3a. The function k denotes the kernel and is a function of four variables: t, s_1,s_2, and U. The term U is shorthand for the input history $\{U(\tau) \mid \tau \in [0,t]\}$, and the terms s_1 and s_2 are a pair of switching values in the Preisach plane, which is shown Figure 3b. We think of s_1 as describing when the hystereic output "jumps down" and s_2 as describing when the output "jumps up". Each kernel depends on two distinct switches s_1 and s_2 and the associated bounding functions γ_{s_1} and γ_{s_2}. The bounding functions describe how smoothly the output jumps up or down at the switching values, as shown in Figure 3a. The value of k is given by

$$k(s_1, s_2, t_n, U) = \begin{cases} \max\{k^{(n-1)}, \gamma_{s_1}(U(t))\} & \text{if } U \text{ is increasing over } [t_{n-1}, t_n], \\ \min\{k^{(n-1)}, \gamma_{s_2}(U(t))\} & \text{if } U \text{ is decreasing over } [t_{n-1}, t_n]. \end{cases}$$

The bounding functions in this paper, γ_{s_1} and γ_{s_2}, are derived from a single envelope function γ and are defined, respectively, as follows:

$$\gamma_{s_1}(\cdot) = \gamma(\cdot - s_1),$$
$$\gamma_{s_2}(\cdot) = \gamma(\cdot - s_2).$$

For the Krasnoselskii–Pokrovskii model [19], the envelope function $\gamma(u)$ is represented by

$$\gamma(u) = tanh(U/a).$$

Here, the parameter $a > 0$ defines the scaling factor applied to the envelope function.

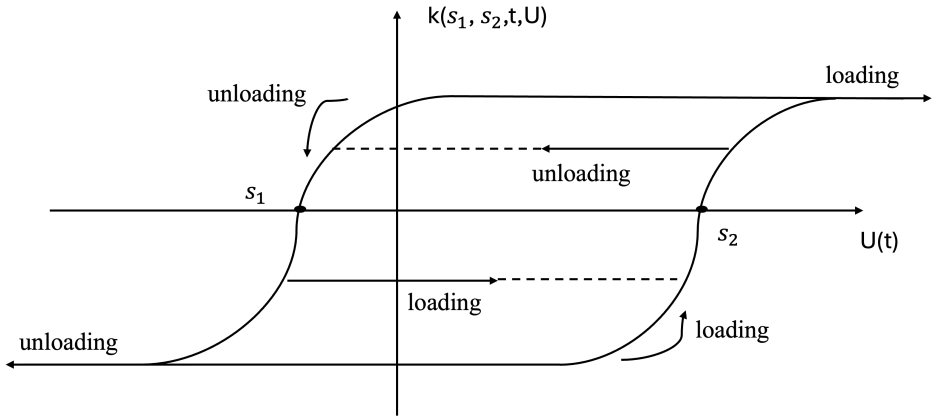

(**a**) A typical hysteresis kernel $k(s_1, s_2, t, U)$ for the part of switches $(s_1, s_2) \in S_\Omega$, where S_Ω is the Preisach plane.

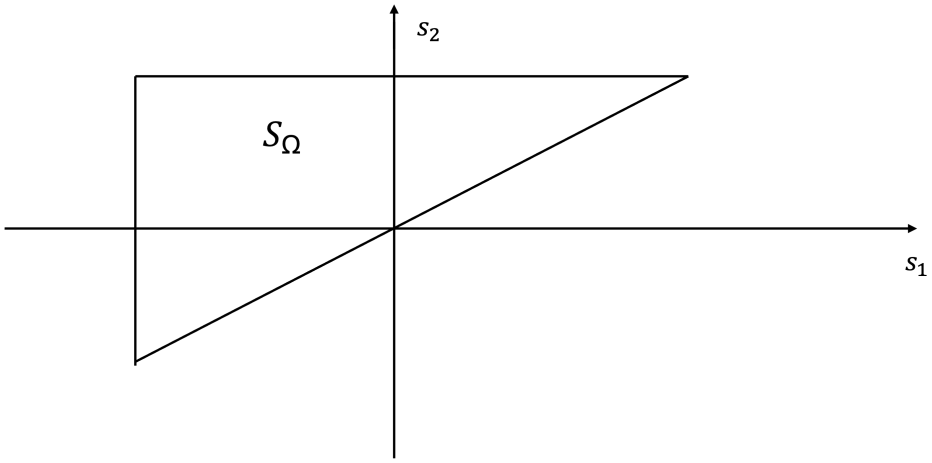

(**b**) The Preisach plane S_Ω. Any point $(s_1, s_2) \in S_\Omega$ defines a hysteresis kernel $k(s_1, s_2, t, U)$.

Figure 3. Illustrations of the Preisach hysteresis modeling framework. (**a**) A typical elementary hysteresis kernel $k(s_1, s_2, t, U)$ associated with a single pair of switching thresholds (s_1, s_2) on the Preisach plane. The kernel switches between two states (loading and unloading) based on the current value of the input $U(t)$ relative to the thresholds. The dashed arrows indicate memory-dependent switching behavior and the formation of hysteresis loops. (**b**) The Preisach plane Ω, which is the set of all valid switching threshold pairs satisfying $s_1 \leq s_2$. Each point $(s_1, s_2) \in \Omega$ defines a hysteresis kernel. The full hysteresis response is obtained by integrating the weighted contributions of these kernels across the Preisach plane.

The operator H, when acting on the input U, is mathematically represented by

$$V(t) = (HU)(t) = \iint_{S_\Omega} k(s_1, s_2, t, U)\mu(\mathrm{d}s_1\, \mathrm{d}s_2). \tag{24}$$

where $k(s_1, s_2, t, U)$ is the fundamental hysteresis kernel introduced in [19,28] and μ is some given measure over the subset S_Ω of the Preisach plane. The subset S_Ω of the Preisach plane is depicted in Figure 3a. This model is sometimes referred to as the generalized play operator or the Krasnoselskii–Porovskii (KP) operator [16].

It should be noted that this hysteresis operator is quite general and depends on a number of real parameters as well as distributed (or functional) parameters. Distributed parameters are not real numbers; rather, they are functions. Distributed parameters reside in a generally infinite dimensional space of functions. The real parameters include the scaling factor a in the definition above of the envelope function $\gamma(u)$, as well as the thresholds α, β that define the subset S_Ω. The distributed parameters include the choice of the envelope function $\gamma(u)$ and the weight $\mu_{jk}(ds_1, ds_2) \triangleq \mu(s_1, s_2)ds_1 ds_2$.

Given the inherent complexity of the KP model, as outlined in Equation (24), approximations must be used for practical algorithms. This is accomplished by discretizing the Preisach plane as depicted in Figure 4 [19].

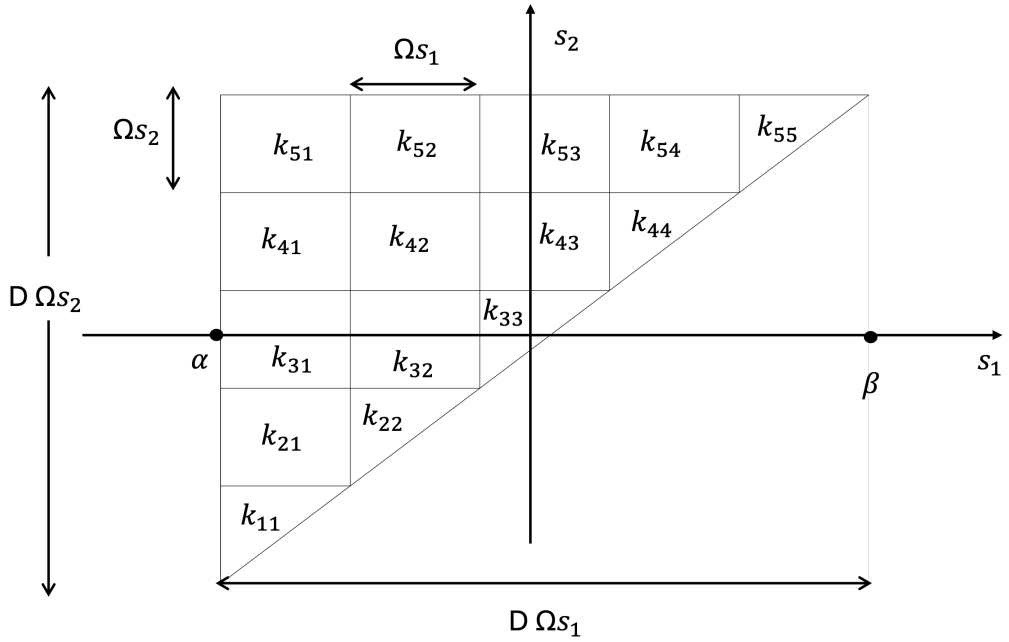

Figure 4. Discretization of the Preisach plane Ω illustrating the distribution of elementary hysteresis switches for a resolution parameter $D = 5$. The plane $\Omega \subset \mathbb{R}^2$ is defined by all pairs (s_1, s_2) satisfying $s_1 \leq s_2$. It is partitioned into triangular subregions, each associated with a hysteresis kernel k_{ij}. The horizontal and vertical axes correspond to the switching thresholds s_1 and s_2, respectively, and the total number of kernel elements is determined by the discretization level D. The thresholds α and β denote the lower and upper bounds of the input domain. The diagonal boundary $s_1 = s_2$ separates admissible kernel regions from non-physical configurations. This discretized structure enables efficient numerical implementation of the Preisach-type hysteresis operator.

We correspondingly introduce the discrete approximation

$$V_D(t) = \sum_{k=1}^{D} \sum_{j=k}^{D} k_{jk}(t)\mu_{jk}\Omega s_1 \Omega s_2. \tag{25}$$

The voltage V_D is an approximation of the output voltage V of the exact hysteresis operator above. The term $k_{jk}(t) := k((s_j, s_k), t, U)$ denotes the evaluation of the KP kernel at the pair $s = (s_j, s_k)$, while $\mu_{jk}\ \Omega s_1 \Omega s_2$ is a discrete weight used to approximate the integral over the subregion Ω_{jk} shown in Figure 4. The discrete parameters Ωs_1 and Ωs_2 are defined as follows:

$$\Omega s_1 = \Omega s_2 = \frac{\alpha - \beta}{D},$$

where α and β are the upper and lower thresholds of the Preisach plane, respectively. This method of discretization is depicted in the Preisach plane in Figure 3b. This plane is divided into $\frac{D(D+1)}{2}$ distinct subsets Ω_{jk}.

This means that the approximation of the hysteresis operator that generates V_D depends on $D(D+1)/2 + 4$ real parameters $\mu_{jk}, \alpha, \beta, a$.

3. Numerical Examples

To illustrate the dynamic behavior of the piezoelectric system under various operating conditions, we present a series of numerical examples. These examples are simulated using the state-space representation and hysteresis model outlined in the previous sections. The numerical simulations were performed using Simulink, which was implemented with the fixed time-stepping algorithm to facilitate modeling nonlinear hysteresis effects; hysteresis modeling using adaptive time-step methods is considerably more complicated to implement. The fixed step size was chosen to be 0.001, and all simulations were carried out using the Matlab R2024b solver `ode14x`. The goal of these simulations was to understand how different input voltages and system parameters affected the tip displacement and velocity of the piezoelectric system and the effect on the hysteresis loop.

The fundamental parameters used for the simulations, including the dimensions and material properties of the substrate and piezoelectric components, are detailed in Table 1. The parameters defining the hysteresis operator H are summarized in Table 2.

Table 1. Basic parameters for substrate and piezoelectric material. The parameters $I = bh^3/12$, $A = bh$.

Parameter	Description	Substrate	Piezoelectric
L_b	Length (mm)	24.06	24.06
b	Width (mm)	6.4	6.4
h	Thickness (mm)	0.14	0.265
ρ	Density (kg/m^3)	9000	7500
C^E	Modulus of Elasticity (GPa)	105	60.6
e	Piezoelectric Constant (C/m^2)	-	-16.6
ε	Permittivity Constant (nF/m)	-	25.55

Table 2. Parameters that define H.

Parameter	Description	Parameter Type	Value
a	Scaling factor	Real	0.4–20
α	Upper bound of Preisach plane	Real	50
β	Lower bound of Preisach plane	Real	-50
γ	Envelope function	Distributed	$\tanh(\cdot)$
μ	Measure that defines hysteresis operator	Distributed	$\mu_{jk} * \Omega_{s_1} * \Omega_{s_2}$
D	Dimension of discretization	Integer	25
Ω_s	Mesh width on Preisach plane	Real	$\frac{\alpha-\beta}{D}$
μ_{jk}	jk^{th} discrete measure over Preisach plane	Real	0.001–0.005

In reviewing these tables, it is important to note that the FDE in its original form does indeed, as claimed in the introduction, depend on a large number of material, structural, and geometric real parameters. Even if the geometry and material parameters are well known or can be determined with relatively high accuracy, the measure μ and envelope function γ are distributed parameters that are phenomenological and hence never known a priori. If we employ online identification or control methods, such as in [17,28], the governing evolution equations can be to the order of

$$O(N + 11 + D^2)$$

time-varying estimates. In the case study, the typical values of N range between 10 and 100, while $D = 25$. We should also point out that it is usually problematic to determine the damping matrix C by upscaling the (micro)mechanical material properties, and it is often considered an important source of uncertainty in the original equations.

To calculate the damping coefficient C, in this paper, we employed the simple proportional damping approach of Rayleigh damping, which is defined as follows:

$$C_{ij} = C_m \mathbb{M}_{ij} + C_k \mathbb{K}_{ij}.$$

In this equation, C_m is a constant number that multiplies the entries of the mass matrix $\mathbb{M}$, and C_k is a constant that multiplies the entries of the stiffness matrix $\mathbb{K}$. This method allows for a combination of mass-proportional and stiffness-proportional damping.

In our assessment via this case study, the system is driven by a range of input voltages to demonstrate the effects on the tip displacement and velocity. The input voltage to the system was chosen to be

$$U = V_{\text{amp}} \sin(\omega t), \tag{26}$$

where V_{amp} is the input voltage and ω is the angular frequency. The limit cycles observed in the tip displacement versus tip velocity plots provide insights into the energy transfer within the system as well as the inherent damping due to the piezoelectric material and the structural dynamics. Table 3 provides an overview of the system parameters used in the simulation.

In this study, we chose the output variables of the dynamic system to represent the tip behavior of the piezoelectric composite beam. Specifically, the first output is defined as the tip displacement, and the second output is the corresponding tip velocity:

$$y_1(t) := \text{tip displacement}, \tag{27}$$

$$y_2(t) := \text{tip velocity}. \tag{28}$$

These outputs are used throughout the numerical examples to characterize the dynamic response of the system. In particular, the limit cycle plots are generated by projecting the system trajectory onto the (y_1, y_2) phase plane, providing insight into the energy dissipation and nonlinear memory effects induced by the hysteresis operator.

Table 3. System parameters used in simulation.

Symbol	Parameter	Value
V_{amp}	Input voltage amplitude (volts)	90–230
ω	Angular velocity (rad/s)	1
C_m	Constant number that multiplies the entries of the mass matrix (1/s)	10
C_k	Constant number that multiplies the entries of the stiffness matrix (s)	10^{-7}

3.1. Effect of Maximum Input Voltage

To understand the effect of the input voltage, we changed the voltage amplitude in Table 3 from 90 volts to 230 volts in increments of 20 volts. As the voltage increased, the system exhibited a higher tip velocity, indicating a larger energy input into the system. This is evident from the expansion of the limit cycles in the displacement-velocity phase plane, depicted in Figure 5. The limit cycles became progressively larger with an increased input voltage, suggesting that the system moves further from its equilibrium position before the restoring forces bring it back, consistent with higher energy states. The hysteresis effect was more apparent at higher voltages because the input voltage $U(t)$ was more significantly shaped by the hysteresis operator $H(U)$, which led to a larger history-dependent response. This caused the limit cycles to become larger and more pronounced as the voltage increased, highlighting the stronger shaping effect of the hysteresis. Figure 5 illustrates the limit cycles for four selected input voltages, capturing the system's transition through different dynamic regimes.

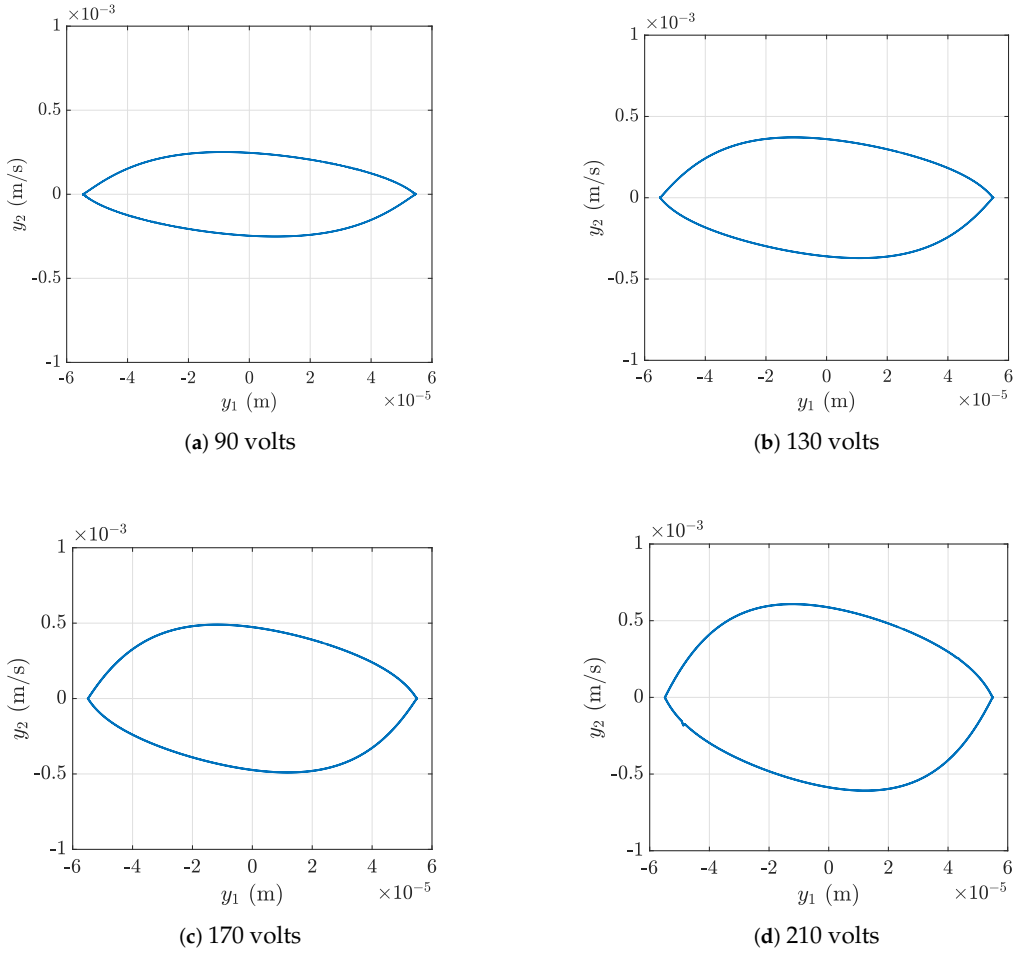

(**a**) 90 volts (**b**) 130 volts

(**c**) 170 volts (**d**) 210 volts

Figure 5. Phase-plane representation of limit cycle behavior in the output response of the piezoelectric beam system under sinusoidal input. Each subfigure shows the trajectory in the (y_1, y_2) plane, where y_1 is the tip displacement and y_2 is the tip velocity. The plots correspond to different input voltage amplitudes: (**a**) 90 volts, (**b**) 130 volts, (**c**) 170 volts, and (**d**) 210 volts. As the input voltage increased, the size of the limit cycle grew, reflecting stronger nonlinear effects induced by the hysteresis operator.

3.2. Effect of Scaling Factor

The scaling factor a in Table 2 that defines the size of the envelope of the hysteresis kernel is crucial for modulating the hysteresis loop, particularly in terms of its effect on the smoothness of the loop and, consequently, the system's limit cycle properties. The

variation in the configuration of the hysteresis loop with respect to different scaling factor values is depicted in Figure 6. It was observed that an increase in the scaling factor resulted in a more gradual transition within the hysteresis loop, giving it a smoother appearance. Conversely, smaller values of a imparted a pronounced, ridge-like structure to the loop. This phenomenon is inherently linked to the formulation of the enveloping function $\gamma(u) = \tanh(U/a)$. As a decreases, γ asymptotically approaches either 1 or -1, signifying a binary state. On the other hand, an increase in a allows γ to adopt a continuum of values within the interval $[-1, 1]$, facilitating a more nuanced modulation of the hysteresis loop.

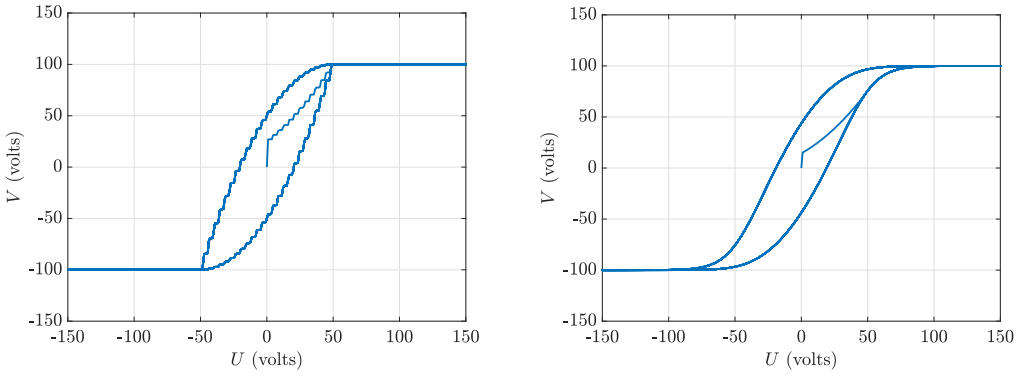

(**a**) (**b**)

Figure 6. Hysteresis loops generated by the Preisach-type operator for different values of the scaling factor a. Here, $U(t)$ is the input voltage, and $V(t) = \mathbf{H}(U)(t)$ is the hysteresis operator output. Subfigure (**a**) corresponds to $a = 0.4$, and (**b**) corresponds to $a = 20$. As the scaling factor increases, the hysteresis loop becomes smoother and more gradual due to the influence of the envelope function $\gamma(U) = \tanh(U/a)$, which governs the range of admissible kernel weights. Smaller values of a yield sharper transitions and a more ridge-like appearance, approximating binary switching behavior. This modulation of smoothness impacts the overall dynamics and limit cycle shape of the system.

In Figure 7, the effect of the scaling factor a on the system's limit cycles is illustrated, with the voltage V and kernel weight μ_{jk} remaining constant. At smaller values of a, the limit cycle exhibits significant nonlinearity, as reflected by the extensive velocity amplitude, indicative of a dynamic system response. As a increases, the limit cycle transitions to a smoother profile, indicative of reduced nonlinearity. This transition reveals the smoothing effect of the scaling factor on the system's oscillations, leading to a stable and periodic limit cycle that signifies a more steady state of the dynamical system.

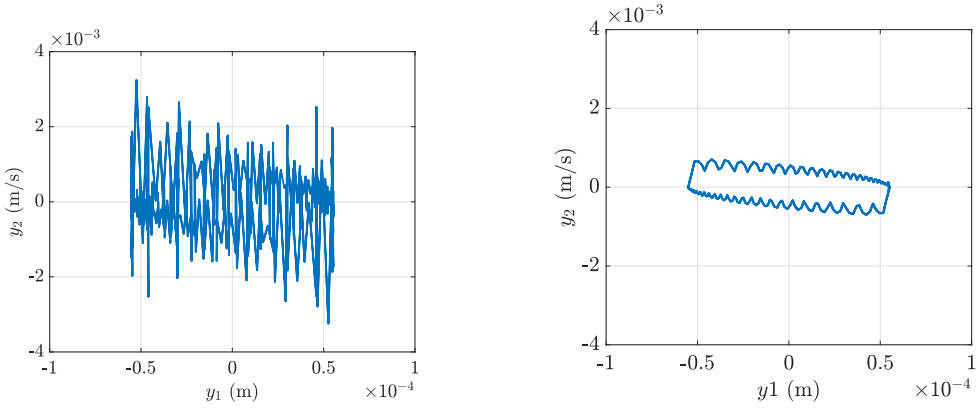

(**a**) $a = 1$ (**b**) $a = 2$

Figure 7. *Cont.*

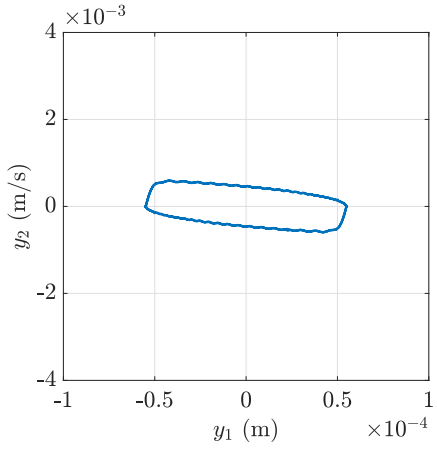

(**c**) $a = 3$

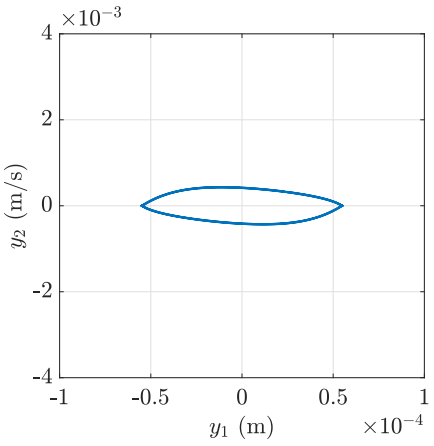

(**d**) $a = 20$

Figure 7. Limit cycle responses in the phase plane (y_1, y_2) for a fixed input voltage $U = 150$ volts and constant kernel weight $\mu_{jk} = 0.02$ under varying values of the hysteresis scaling factor a. Subfigures (**a**–**d**) correspond to $a = 1, 2, 3$, and 20, respectively. As a increases, the hysteresis effect smooths out, resulting in more stable limit cycles.

3.3. Effect of Kernel Weight μ_{jk}

The modulation of hysteresis behavior and associated limit cycles by the kernel weight is depicted in Figure 8. Variations in the kernel weight μ_{jk} in Table 2 influence the amplitude of the hysteresis operator's output, directly influencing the dynamic system's response and thereby altering the observed limit cycles.

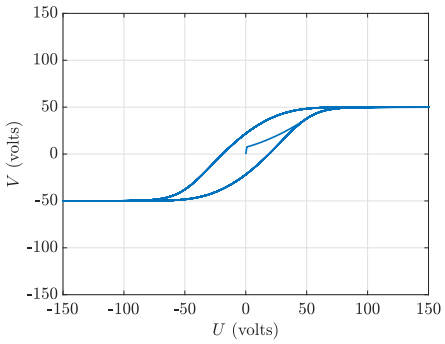

(**a**) $\mu = 0.01$

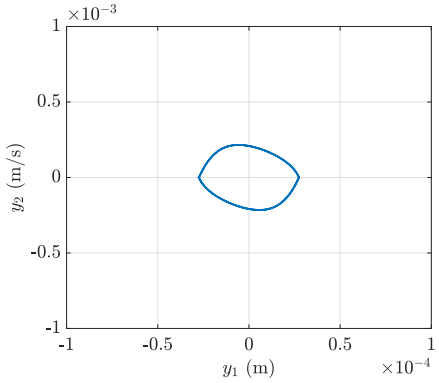

(**b**) Phase portrait for $\mu = 0.01$

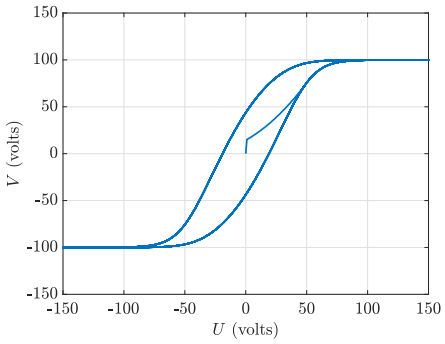

(**c**) $\mu = 0.02$

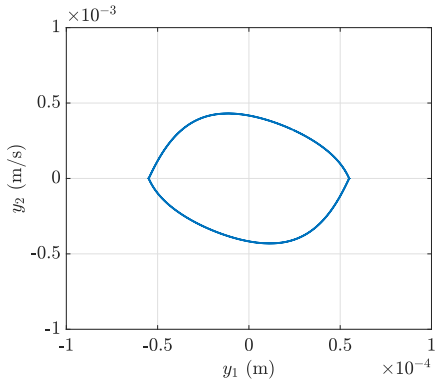

(**d**) Phase portrait for $\mu = 0.02$

Figure 8. *Cont.*

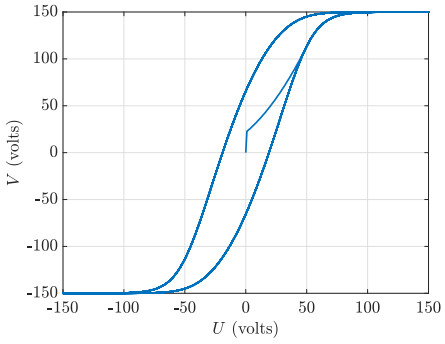

(**e**) $\mu = 0.03$

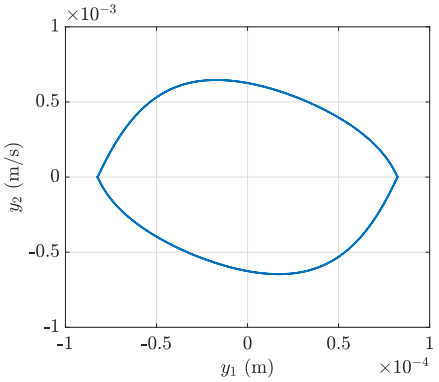

(**f**) Phase portrait for $\mu = 0.03$

Figure 8. Effect of the kernel weight μ_{jk} on the hysteresis loop (left column) and corresponding limit cycle response (right column) in the phase plane (y_1, y_2). The input voltage is $U = 150$ volts, and the scaling factor is fixed.

3.4. Effect of Switching Parameters α and β

The switching parameters α and β play a fundamental role in the behavior of the KP hysteresis model. These parameters define the thresholds at which individual relay operators within the Preisach plane switch states in response to changes in the input voltage.

The function μ represents a distributed measure over the Preisach plane, which incorporates the kernel weight, kernel size, and other scaling characteristics of the model. A component of this distributed measure, the kernel weight μ_{jk}, determines the contribution of a specific Preisach cell located at (s_1^j, s_2^k) to the overall hysteretic output.

While μ collectively governs the intensity and shape of the hysteresis loop, the switching parameters α and β determine which regions of the Preisach plane are active during the input cycle. Consequently, fixing the kernel weight μ_{jk} while varying α and β can significantly influence the hysteresis response. In particular, if the switching thresholds are too narrow relative to the input signal range, the hysteretic memory may be underutilized, leading to a response that does not fully represent the physical system.

To explore this effect, we fixed the input voltage amplitude at $U = 170$ volts and set the kernel weights uniformly as $\mu_{jk} = 0.02$. We then varied the switching thresholds α and β to examine their impact on both the hysteresis loop and the associated limit cycle, as shown in Figure 9.

Figure 9 illustrates the influence of the switching parameters α and β on both the hysteresis loop (left) and the resulting limit cycle (right) for a fixed input amplitude of $U = 170$ V. In case (a), with a wide switching range ($\alpha = -40$, $\beta = 80$), the hysteresis loop exhibited broad saturation regions. Specifically, the output voltage V remained flat at approximately -200 V when the input U was between -170 V and -80 V and saturated at approximately $+200$ V when U was between $+100$ V and $+170$ V. The corresponding limit cycle exhibited a relatively large amplitude in terms of both displacement and velocity, with y_1 ranging between -1×10^{-4} m and 1×10^{-4} m and y_2 ranging between -0.7×10^{-3} m/s and 0.7×10^{-3} m/s.

In contrast, case (b) used narrower switching thresholds ($\alpha = -20$, $\beta = 30$), which confined the active Preisach region. The resulting hysteresis loop was less saturated, with the output voltage V plateauing at approximately -25 V for inputs $U \in [-170, -40]$ and at $+25$ V for $U \in [50, 170]$. This limited hysteresis effect led to a significantly smaller limit cycle, with the displacement y_1 ranging from -1.5×10^{-5} m to 1.5×10^{-5} m and the velocity y_2 ranging from -1.5×10^{-4} m/s to 1.5×10^{-4} m/s.

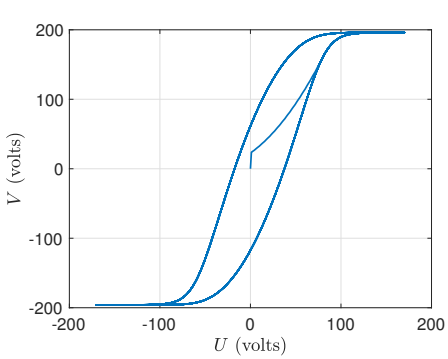

(**a**) $\alpha = -40$, $\beta = 80$

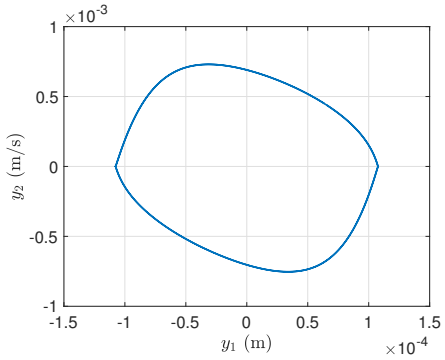

(**b**) Limit cycle for $\alpha = -40$, $\beta = 80$

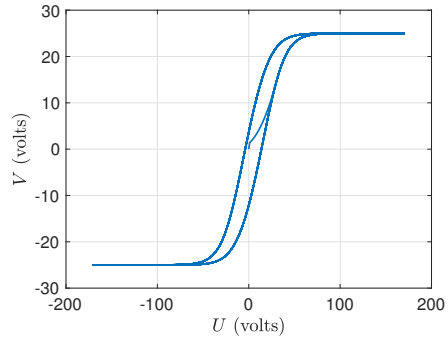

(**c**) $\alpha = -20$, $\beta = 30$

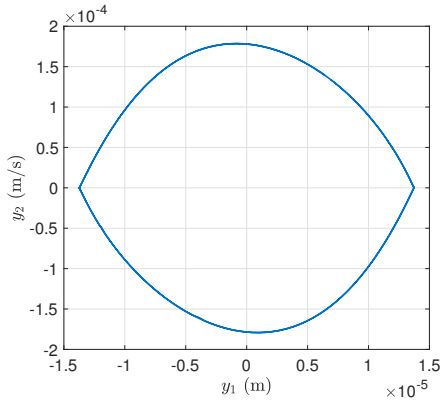

(**d**) Limit cycle for $\alpha = -20$, $\beta = 30$

Figure 9. Comparison of hysteresis loops (left) and corresponding limit cycle responses (right) for a fixed input voltage amplitude $U = 170$ volts under two different sets of hysteresis switching thresholds α and β. Subfigures (**a**,**b**) correspond to $\alpha = -40$, $\beta = 80$, and subfigures (**c**,**d**) correspond to $\alpha = -20$, $\beta = 30$. Wider thresholds resulted in broader loops and larger oscillations, while narrower thresholds localized the response.

These results highlight how reducing the switching interval can dramatically compress the output range and attenuate the system's nonlinear dynamic response.

4. Discussion

The numerical examples presented in the previous section illustrate how the parameters of the discretized hysteresis operator influenced the dynamic behavior of a piezoelectric beam system. Several key insights emerged from these simulations:

- The system exhibited strongly nonlinear behavior, including memory-dependent limit cycles, under sinusoidal actuation. This arose not from geometric or material nonlinearities in the beam itself but from the hysteretic transformation of the input signal by the KP operator.
- The shape and amplitude of the limit cycles were highly sensitive to the parameters of the hysteresis model, including the scaling factor a, kernel weight μ_{jk}, and switching thresholds α, β. These parameters controlled not only the strength of the nonlinearity but also its frequency-dependent shaping effect on the system response.
- Because the hysteresis operator was discretized over the Preisach plane, the resulting system depended on a large number of real and distributed parameters. Combined with the high-dimensional state-space representation from modal reduction, the model

has a complexity that poses practical challenges for identification, control, and real-time simulation.

Experimental identification of such systems is particularly challenging due to several intrinsic complexities:

1. History-dependent and nonlinear input–output behavior;
2. High-dimensional state-space representations resulting from modal discretization;
3. Dependence on a large number of real-valued parameters in the hysteresis model;
4. Reliance on generally infinite-dimensional distributed parameters.

In particular, the parameters that define phenomenological hysteresis operators, such as Preisach or KP-type kernels, are rarely known a priori and are difficult to infer directly from measured data. These factors justify a modeling approach centered on numerical simulations and motivate the use of surrogate or data-driven modeling strategies.

Overall, while the proposed model captures nonlinear memory effects, it remains computationally intensive and highly sensitive to parameter selection. These challenges underscore the need for reduced-order modeling techniques that preserve essential hysteretic dynamics while lowering the computational burden. One promising direction is the use of operator-theoretic frameworks such as Koopman operator theory to approximate the system behavior with fewer degrees of freedom. These directions are pursued in follow-up work.

The modeling framework developed in this work is well suited for a range of practical applications where accurate representation of hysteretically nonlinear piezoelectric behavior is critical. In particular, the ability to capture memory-dependent effects in distributed-parameter systems enables more reliable prediction and control in engineering scenarios such as precision motion control, where sub-micrometer accuracy is required in nanopositioning systems and scanning probe microscopy; vibration suppression in smart structures used in aerospace and civil engineering, where piezoelectric layers are employed for active damping; and energy harvesting systems, such as MEMS devices and structural harvesters, where accurate modeling is necessary to optimize power output under nonlinear dynamic conditions. By embedding hysteresis effects directly into the governing equations, the model forms a foundation for reduced-order modeling, control synthesis, and data-driven extensions aimed at real-world deployment in smart material systems.

Several limitations of the present study suggest opportunities for future work. First, the hysteresis operator parameters were selected to illustrate qualitative behaviors rather than being fitted to experimental data; parameter identification and data-driven model calibration remain important open challenges. Second, the analysis was limited to sinusoidal actuation signals; evaluating the system's response under broadband or stochastic inputs would offer a more complete understanding of its dynamic behavior. Third, the current model is restricted to a one-dimensional beam; extending the framework to plate-like or three-dimensional piezoelectric structures would pose new challenges in both discretization and computational efficiency. Lastly, integrating this modeling approach with feedback control schemes and investigating model reduction or hybrid modeling techniques for real-time implementation remain promising directions for future investigation.

5. Conclusions

This work presents a comprehensive modeling framework for piezoelectric composite beams with hysteresis by coupling a distributed-parameter structural model with a nonlinear hysteresis operator. A Krasnosel'skii–Pokrovskii (KP) formulation is used to represent rate-independent hysteresis in a physically meaningful and flexible way. By discretizing the Preisach plane and applying modal expansion to the beam dynamics, the full system is expressed as a high-dimensional functional differential equation (FDE) that captures key

hysteretic phenomena such as memory, path dependence, and saturation. The resulting model depends on a large number of structural modes and a distributed set of parameters defining the hysteresis operator, making it computationally intensive and challenging for control design, identification, and real-time implementation.

These observations underscore the need for effective reduced-order modeling strategies that can preserve the essential dynamics while significantly lowering computational cost and model complexity. In particular, data-driven techniques such as Koopman operator theory offer promising avenues for constructing low-dimensional approximations of complex nonlinear systems like the one studied here. Future work will investigate the use of operator-theoretic methods to learn predictive models directly from simulated or experimental data, with the aim of developing efficient surrogate models that retain the memory effects and input–output behavior of the original FDE system.

Author Contributions: Conceptualization, A.H.A. and A.J.K.; methodology, A.H.A. and A.J.K.; writing—original draft preparation, A.H.A.; writing—review and editing, A.H.A. and A.J.K.; supervision, A.J.K. All authors have read and agreed to the published version of the manuscript.

Funding: This research received no external funding.

Data Availability Statement: The data supporting the findings of this study were generated via numerical simulation and are available from the corresponding author upon reasonable request.

Conflicts of Interest: The authors declare no conflicts of interest.

References

1. Banks, H.; Smith, R.; Wang, Y. *Smart Material Structures Modeling, Estimation, and Control*; Wiley: Mason, Paris, 1996.
2. Tichy, J.; Erhart, J.; Kittinger, E.; Privratska, J. *Fundamentals of Piezoelectric Sensorics*; Springer, Inc.: Berlin, Germany, 2010.
3. Yang, J. *Introduction to the Theory of Piezoelectricity*; Springer: New York, NY, USA, 2005.
4. Yang, J. *Mechanics of Piezoelectric Structures*; Springer: New York, NY, USA, 2020.
5. Kurdila, A.J.; Tarazaga, P.A. *Vibrations of Linear Piezostructures*; Wiley: Blacksburg, VA, USA, 2021.
6. Erturk, A.; Inman, D.J. *Piezoelectric Energy Harvesting*; Wiley: Hoboken, NJ, USA, 2011.
7. Tiersten, H.F. *Linear Piezoelectric Plate Vibrations: Elements of the Linear Theory of Piezoelectricity and the Vibrations of Piezoelectric Plates*; Plenum Press: New York, NY, USA, 1969.
8. Maugin, G.A. *Nonlinear Electromechanical Effects and Applications*; Series in Theoretical and Applied Mechanics; World Scientific Pub: Singapore, 1985; Volume 1.
9. Stanton, S.C.; Erturk, A.; Mann, B.P.; Inman, D.J. Nonlinear piezoelectricity in electroelastic energy harvesters: Modeling and experimental identification. *J. Appl. Phys.* **2010**, *108*, 074903. [CrossRef]
10. Leadenham, S.; Erturk, A. Unified Nonlinear Electroelastic Dynamics of a Bimorph Piezoelectric Cantilever for Energy Harvesting, Sensing, and Actuation. *Nonlinear Dyn.* **2015**, *79*, 1727–1743. [CrossRef]
11. Asanuma, H.; Komatsuzaki, T. Nonlinear Piezoelectricity and Damping in Partially-Covered Piezoelectric Cantilever with Self-Sensing Synchronized Switch Damping on Inductor Circuit. *Mech. Syst. Signal Process.* **2020**, *144*, 106867. [CrossRef]
12. Asanuma, H. Selecting Nonlinear Piezoelectricity for Fully Autonomous Self-Sensing Synchronized Switch Damping on Inductor Technique. *Mech. Syst. Signal Process.* **2021**, *159*, 107846. [CrossRef]
13. Lumentut, M.F.; Shu, Y.C. Shunted Optimal Vibration Energy Harvesting Control of Discontinuous Smart Beams. *Compos. Struct.* **2020**, *242*, 112126. [CrossRef]
14. Krasnosel'skii, M.A.; Pokrovskii, A.V. *Systems with Hysteresis*; Springer: Berlin, Germany, 1989.
15. Sabarianand, D.V.; Karthikeyan, P.; Muthuramalingam, T. A Review on Control Strategies for Compensation of Hysteresis and Creep on Piezoelectric Actuators Based Micro Systems. *Mech. Syst. Signal Process.* **2020**, *140*, 106634. [CrossRef]
16. Visintin, A. *Differential Models of Hysteresis*; Springer: Berlin, Germany, 1994.
17. Paruchuri, S.; Guo, J.; Kurdila, A. Reproducing kernel Hilbert space embedding for adaptive estimation of nonlinearities in piezoelectric systems. *Nonlinear Dyn.* **2020**, *101*, 1397–1415. [CrossRef]
18. Gan, J.; Zhang, X. A review of nonlinear hysteresis modeling and control of piezoelectric actuators. *AIP Adv.* **2019**, *9*, 040702. [CrossRef]
19. Li, Z.; Shan, J.; Gabbert, U. Inverse Compensation of Hysteresis Using Krasnoselskii-Pokrovskii Model. *IEEE/ASME Trans. Mechatronics* **2018**, *23*, 966–971.

20. Salah, M.; Saleem, A. Hysteresis Compensation-Based Robust Output Feedback Control for Long-Stroke Piezoelectric Actuators at High Frequency. *Sens. Actuators A Phys.* **2021**, *319*, 112542. [CrossRef]
21. Yu, Z.; Wu, Y.; Fang, Z.; Sun, H. Modeling and Compensation of Hysteresis in Piezoelectric Actuators. *Heliyon* **2020**, *6*, e03999. [CrossRef] [PubMed]
22. von Wagner, U.; Hagedorn, P. Nonlinear effects of piezoceramics excited by weak electric fields. *Nonlinear Dyn.* **2003**, *31*, 133–149. [CrossRef]
23. Dai, Y.; Li, D.; Wang, D. Review on the Nonlinear Modeling of Hysteresis in Piezoelectric Ceramic Actuators. *Actuators* **2023**, *12*, 442. [CrossRef]
24. Xu, Y.; Luo, Y.; Luo, X.; Chen, Y.; Liu, W. Fractional-Order Modeling of Piezoelectric Actuators with Coupled Hysteresis and Creep Effects. *Fractal Fract.* **2024**, *8*, 3. [CrossRef]
25. Li, H.; Tong, Y.; Li, C. Modeling and Control of a Linear Piezoelectric Actuator. *Actuators* **2024**, *13*, 55. [CrossRef]
26. Baziyad, A.G.; Ahmad, I.; Salamah, Y.B. Precision Motion Control of a Piezoelectric Actuator via a Modified Preisach Hysteresis Model and Two-Degree-of-Freedom H-Infinity Robust Control. *Micromachines* **2023**, *14*, 1208. [CrossRef] [PubMed]
27. Inman, D.J. *Engineering Vibration*, 4th ed.; Pearson: Boston, MA, USA, 2014.
28. Dadashi, S.; Bobade, P.; Kurdila, A.J. Online Estimation and Adaptive Control for a Class of History Dependent Functional Differential Equations. *Nonlinear Dyn.* **2018**, *92*, 1431–1451. [CrossRef]

Disclaimer/Publisher's Note: The statements, opinions and data contained in all publications are solely those of the individual author(s) and contributor(s) and not of MDPI and/or the editor(s). MDPI and/or the editor(s) disclaim responsibility for any injury to people or property resulting from any ideas, methods, instructions or products referred to in the content.